

Real-time imaging of acoustic rectification

S. Danworaphong,¹ T. A. Kelf,² O. Matsuda,² M. Tomoda,² Y. Tanaka,² N. Nishiguchi,² O. B. Wright,^{2,a)} Y. Nishijima,³ K. Ueno,³ S. Juodkazis,³ and H. Misawa³

¹*School of Science, Walailak University, Nakhon Si Thammarat 80160, Thailand*

²*Division of Applied Physics, Graduate School of Engineering, Hokkaido University, Sapporo 060-8628, Japan*

³*Research Institute for Electronic Science, CRIS Building, Hokkaido University, Sapporo 001-0021, Japan*

(Received 14 July 2011; accepted 31 October 2011; published online 17 November 2011)

We image gigahertz surface acoustic waves normally incident on a microscopic linear array of triangular holes—a generic “acoustic diode” geometry—with a real-time ultrafast optical technique. Spatiotemporal Fourier transforms reveal wave diffraction orders in \mathbf{k} -space. Squared amplitude reflection and transmission coefficients for incidence on both sides of the array are evaluated and compared with numerical simulations. We thereby directly demonstrate acoustic rectification with an asymmetric structure. © 2011 American Institute of Physics. [doi:10.1063/1.3662930]

Rectifying waves is best known in the context of the electric diode, but the phenomenon is general and applies to any wave field. For example, using nonlinear effects, it is possible to rectify incoherent phonons in the form of heat^{1,2} or coherent phonons in the form of acoustic waves.^{3,4} These rectification effects are important in applications such as thermal and acoustic insulation and also in shock-wave lithotripsy.⁵ Following on from similar calculations in optics,⁶ it was recently shown theoretically that rectification of bulk acoustic waves could be achieved using asymmetric structures such as arrays of triangles without requiring any nonlinearity.^{7,8} In spite of this interest, there have been no experiments to image the passage of a wave field through a rectifier in the time domain. In this letter, we apply an ultrafast real-time optical imaging technique^{9,10} to investigate the transmission and reflection of ~ 1 GHz surface acoustic waves (SAWs) incident on a periodic linear array of microscopic triangular holes, a generic rectifying geometry.

The sample is produced on a Si(100) wafer of thickness 0.5 mm by plasma dry etching with alternate use of SF₆ and C₄F₈ gases—a row of equilateral triangles with circularly truncated vertices, with a pre-truncation side length of 11.9 μm . The diameter of the rounded vertices is 3.2 μm , the array period is $d = 20.3$ μm , and the etched depth is 11.3 μm with vertical walls. A scanning electron micrograph of the sample is shown in Fig. 1(a). The sample is coated with a 30 nm film of polycrystalline chromium to localize the optically excited thermoelastic stress near the sample surface. This thickness does not produce significant acoustic dispersion.¹² We use an optical pump and probe technique combined with a common-path interferometer to image the SAWs.¹¹ The pump (frequency-doubled, wavelength 415 nm, incident pulse energy 0.7 nJ) and probe (wavelength 830 nm, incident pulse energy 0.07 nJ) pulses originate from a mode-locked Ti:Sapphire laser with a 80.4 MHz repetition rate and a 0.2 ps pulse duration. The pump pulses are modulated at 1 MHz for lock-in detection and are reshaped by a cylindrical lens and a $\times 50$ microscope objective lens to produce a line source of full width at half maximum (FWHM)

spatial width ~ 1 μm and aspect ratio 40:1 on the sample surface. The lateral extent of the source was chosen to be as long as practically possible to allow coherent effects of scattered wave overlap, important for rectification, to be observable. Broadband plane SAWs with frequencies 100 MHz–1 GHz and wavelengths 5–60 μm are thermoelastically generated ~ 100 μm away from triangle array. Out-of-plane motion (~ 10 pm in amplitude) is detected with ~ 0.5 pm resolution by two probe pulses at an interval of 300 ps. The 2 μm diameter probe spot is scanned over the sample, and the optical phase difference $\Delta\phi$ between the

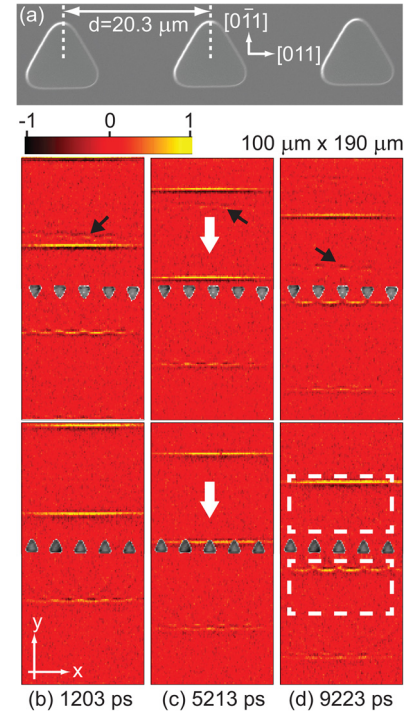


FIG. 1. (Color online) (a) Scanning electron micrograph of the triangle array, showing the Si crystal axes. (b)–(d) show phase ($\Delta\phi$) images at 1203, 5213, and 9223 ps, respectively. The top and bottom images represent different directions of SAW incidence (white arrows). The black arrows show reflected wavefronts. The dashed rectangles represent regions analysed by spatiotemporal Fourier transforms. The gray triangles are superimposed from reflectance images.

^{a)}Electronic mail: aspp@kino-ap.eng.hokudai.ac.jp

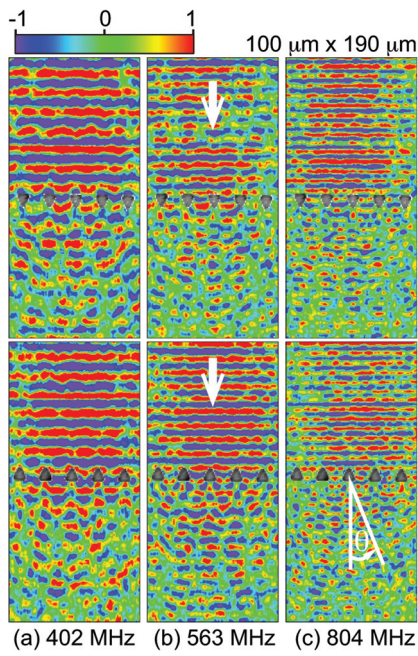


FIG. 2. (Color online) Images of the real part of the temporal Fourier transform at (a) 402 MHz, (b) 563 MHz, and (c) 804 MHz. Arrows identify the incidence, and θ is the diffraction angle.

probe pulses is imaged at a fixed pump-probe delay time τ . By incrementing τ , animations¹³ of 31 frames are obtained within the 12.4 ns laser repetition period. Here $\Delta\phi \propto du_z/dt$, the time derivative of the out-of-plane surface motion. Figures 1(b)–1(d) show SAW images at different delay times for a $100 \times 190 \mu\text{m}^2$ region. The top and bottom images represent SAW incidence on the triangle bases and vertices, respectively. Scattered and reflected wave fronts (see black arrows indicating the latter) are evident, except that the reflection for waves incident on the vertices is small and only shows up clearly in the animations.¹³ The measured wave speed is $v = 5000 \text{ ms}^{-1}$ in the main propagation direction, slightly less than the predicted 5100 ms^{-1} for bare Si owing to film loading.¹⁵

Temporal Fourier transforms reveal the wave fields at individual frequencies, as shown by their real parts in Figs. 2(a)–2(c) for three different frequencies (also shown in animations¹³). Complicated multiple-slit diffraction patterns are evident in reflection and transmission. The diffraction angles θ_n are determined by Bragg's law, $d \sin \theta_n = n\lambda$, where d is the periodicity, λ is the SAW wavelength, and n is the diffraction order, respectively; $\theta_1 \approx 38^\circ$, 26° , and 18° for acoustic frequencies $f = 402$, 563 , and 804 MHz , respectively. These angles are in close agreement with those estimated from experiment.

To elucidate the transmission and reflection processes, two regions of dimensions $72 \times 30 \mu\text{m}^2$ [rectangles in Fig. 1(d)] starting $10 \mu\text{m}$ away from the central line of the triangle array are chosen for analysis:¹⁴ one contains the incident and reflected waves and the other the transmitted waves. The corresponding moduli of the spatiotemporal Fourier transforms for these regions, normalized with respect to the incident waves, are shown in k -space in Figs. 3(a)–3(l). Features corresponding to reflected and transmitted waves lie on the anisotropic constant frequency surfaces for SAWs and

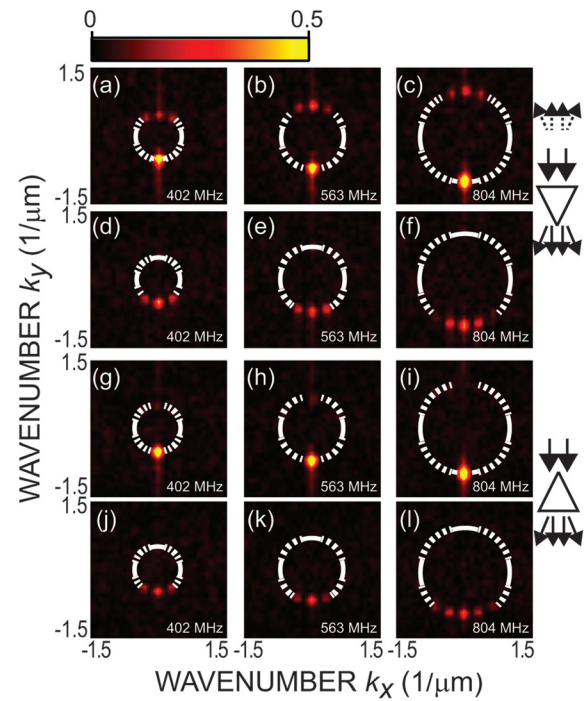


FIG. 3. (Color online) Diffraction viewed in k -space: (a)–(f) and (g)–(l) represent the normalized modulus of the spatiotemporal Fourier transform for incidence on the bases and vertices of the triangles, respectively; (a)–(c) and (g)–(i) refer to the incident regions, and (d)–(f) and (j)–(l) to the transmitted regions. The dashed and solid curves are the SAW and pseudo-SAW constant frequency surfaces, respectively.

pseudo-SAWs of the substrate (see white dashed and solid curves, respectively).^{15–17}

The single bright spots in the first and the third rows in Fig. 3 represent the incident wave fields. The reflection from

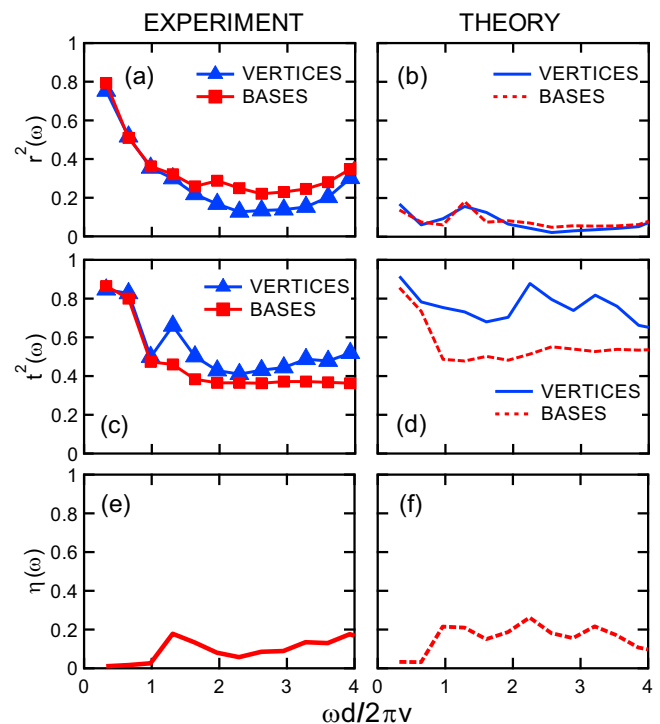


FIG. 4. (Color online) Experimental (a), (c) and simulated (b), (d) reflection and transmission spectra for squared amplitude. (e), (f) The corresponding rectification efficiencies.

the bases (first row) is stronger than that from the vertices (third row), as previously noted. The Bragg condition leads to an n th order only for $f > nv/d$; the thresholds for diffraction orders 1, 2, and 3 to appear are 246, 497, and 739 MHz, respectively. Orders 0-2 are discernible, order 2 only being resolved in Figs. 3(f) and 3(l). The observed horizontal separation in \mathbf{k} -space between diffraction peaks $\Delta k_x = 2\pi/d \approx 0.31 \mu\text{m}^{-1}$ in k_x is constant for all frequencies, as predicted by Bragg's law.

This data in \mathbf{k} -space allow us to evaluate the moduli of the experimental squared amplitude reflection and transmission spectra $r^2(f)$ and $t^2(f)$ corresponding to an experimentally accessible sum of $|du_z/dt|^2$ over all diffraction orders, respectively, shown in Figs. 4(a) and 4(c). Similar curves in Figs. 4(b) and 4(d) are based on finite difference time domain simulations, including the actual hole shape and source width.¹⁸ The horizontal axis is the dimensionless frequency $\omega d/(2\pi v)$ ($= d/\lambda$), where ω is the angular frequency. Geometrical acoustics predicts r^2 to be greater and t^2 to be correspondingly smaller for incidence on the bases compared to that on the vertices.⁷ This is borne out for $\omega d/(2\pi v) > 1$. At low frequencies, where geometrical acoustics is not even approximately applicable, r^2 and t^2 should become equal,⁸ as observed. However, r^2 for incidence on the bases or vertices show an unexpected enhancement at low frequencies in experiment, not reproduced by the theory. This may be caused by the approximations involved in the use of a vertically directed force in the simulations (resulting in a difference in the amount of acoustic energy scattered to bulk waves) or by the neglect of ultrasonic attenuation.¹⁹ For $\omega d/(2\pi v) \gtrsim 1$, experiment and simulation show similar relatively flat responses as a function of frequency. In the experiments and simulations for $t^2(\omega)$, it is, however, evident that the curves show changes in gradient just before the 1st order diffraction threshold [at $\omega d/(2\pi v) = 1$], as seen previously for bulk waves.⁷ These features are, however, not clear at the 2nd and higher-order diffraction thresholds,^{7,8} probably owing to the finite lateral extent of the source and the limited frequency resolution.

The data may be plotted in terms of an effective rectification efficiency $\eta(\omega) = (t_B^2(\omega) - t_V^2(\omega))/(t_B^2(\omega) + t_V^2(\omega))$, where $t_{V,B}^2(\omega)$ are the squared moduli of the amplitude transmission coefficients for propagation toward the vertices (V) and bases (B), respectively. The overall variations of $\eta(\omega)$

for experiment and theory, shown in Figs. 4(e) and 4(f), are similar, both varying from a low frequency value of near zero⁸ to values $\eta \sim 0.2$. Further experiments on a range of source widths, angles of incidence, and hole depths as well as different geometries, including double rows of triangles,^{6,8} would be valuable to elucidate this rectification effect and optimize its efficiency. Experimental work on bulk waves would also be welcome.

In conclusion, we have measured real-time SAW reflection and transmission from a linear array of microscopic triangular holes. The rectification efficiency η shows an "acoustic diode" effect, reproduced approximately by theory. Generalization to two-dimensional arrays of pyramids or prisms⁶ is feasible, with possible use as acoustic one-way mirrors. Moreover, when shrunk to the nanoscale, such structures could find application as thermal rectifiers.

¹C. Starr, J. Appl. Phys. **7**, 15 (1935).

²C. W. Chang, D. Okawa, A. Majumdar, and A. Zettl, *Science* **314**, 1121 (2006).

³B. Liang, B. Yuan, and J.-C. Cheng, Phys. Rev. Lett. **314**, 1121 (2009).

⁴B. Liang, B. Yuan, and J.-C. Cheng, *Nature Mater.* **9**, 989 (2010).

⁵S. Zhu, T. Dreyer, M. Liebler, R. Riedlinger, G. M. Pleminger, and P. Zhong, *Ultrasound Med. Biol.* **30**, 675 (2004).

⁶H. Kim and B. Lee, *Opt. Eng.* **45**, 084004 (2006).

⁷S. Shirota, R. Krishnan, Y. Tanaka, and N. Nishiguchi, *Jpn. J. Appl. Phys.* **46**, L1025 (2007).

⁸R. Krishnan, S. Shirota, Y. Tanaka, and N. Nishiguchi, *Solid State Commun.* **144**, 194 (2007).

⁹Y. Sugawara, O. B. Wright, O. Matsuda, M. Takigahira, Y. Tanaka, S. Tamura, and V. E. Gusev, *Phys. Rev. Lett.* **88**, 185504 (2002).

¹⁰Y. Sugawara, O. B. Wright, and O. Matsuda, *Appl. Phys. Lett.* **83**, 1340 (2003).

¹¹T. Tachizaki, T. Muroya, O. Matsuda, Y. Sugawara, D. H. Hurley, and O. B. Wright, *Rev. Sci. Instrum.* **77**, 043713 (2006).

¹²G. W. Farnell and E. L. Adler, in *Physical Acoustics*, edited by W. P. Mason and R. N. Thurston (Academic, New York, 1972), Vol. **9**, p. 35.

¹³See supplementary material at <http://dx.doi.org/10.1063/1.3662930> for animations.

¹⁴The length of the analysed region in the y direction was chosen to be smaller than the SAW beam width to minimize far-field diffraction effects.

¹⁵T. Aono and S. Tamura, *Phys. Rev. B* **55**, 6754 (1997).

¹⁶R. E. Vines, M. R. Hauser, and J. P. Wolfe, *Z. Phys. B* **98**, 255 (1995).

¹⁷Y. Sugawara, O. B. Wright, and O. Matsuda, *Rev. Sci. Instrum.* **74**, 519 (2003).

¹⁸The grid size is $0.34 \mu\text{m}$ in space and 0.4 ps in time, over a time of 12.4 ns , including the effect of multiple pulses. A normal line source impulse was used with a Gaussian form in the x and y directions with FWHM spatial widths 1 and $40 \mu\text{m}$, respectively. The Cr film was not included.

¹⁹The measured attenuation coefficient is $0.03 \mu\text{m}^{-1}$.